Energy Advances

ROYAL SOCIETY OF CHEMISTRY

PAPER

View Article Online
View Journal | View Issue

Check for updates

Cite this: *Energy Adv.*, 2025, 4, 1267

Slug-flow-based continuous manufacturing of Fe-substituted Ni-rich NCM cathodes for lithium-ion batteries: synthesis and modeling

Arjun Patel,[a] Michael L. Rasche,[a] Sourav Mallick,[a] Sunuk Kim,[a] Mo Jiang,[a] Mariappan Parans Paranthaman,[b] Herman Lopez[c] and Ram B. Gupta *[a]

Received 8th February 2025,
Accepted 10th August 2025

DOI: 10.1039/d5ya00032g

rsc.li/energy-advances

Continuous production of good quality low-cobalt Ni-rich cathode is needed as it can offer high capacity suitable for electric vehicles. However, the low-cobalt NCM-based materials suffer from a high cation mixing and poor rate capability. Also, proper optimization of co-precipitation reaction parameters as well as the manufacturing platform are needed to obtain NCM-precursor particles with uniform particle size and morphology. In order to address all the issues, in this work, a slug-flow-based manufacturing platform is utilized for the continuous production of Fe^{3+} substituted $Ni_{0.85}Co_{(0.1-x)}Mn_{0.05}Fe_xC_2O_4$ (where x = 0, 0.02, 0.04) precursors. The slug-flow manufacturing produces precursor particles with high yield and uniformity. The effect of reactants concentration on the product yield and composition is analyzed through mathematical modelling. Finally, the electrochemical performance of the Ni-rich cathodes with various amounts of Co and Fe content is analyzed through rate capability, cycling stability, and impedance analysis. This work provides key insight into: (i) reactor design for continuous production; (ii) mathematical modelling of the precipitation reaction parameter; and (iii) a detail study of the effect of Co-substitution with Fe^{3+} in Ni-rich NCM on its physical properties as well as electrochemical performance. We find that an intermediate Fe content provides optimum cathode with desired properties.

1. Introduction

Rechargeable lithium-ion batteries (LIB) are heavily used in portable electronic devices and electric vehicles (EVs) due to their higher volumetric and gravimetric energy densities compared to other battery technologies.[1–3] Current LIBs have come a long way since their first introduction in 1991 by Sony, with two to three-fold increase in the energy density at cell level (*e.g.*, volumetric energy density increased from 220 to 700 Wh L^{-1} and gravimetric energy density from 98 to 300 Wh kg^{-1}).[4] Since the invention of LIBs, there has been extensive research on every component of the LIBs with a particular focus on the cathodes because of their high cost and bottleneck in achieving a high capacity compared to commonly used graphite anode which can deliver a specific capacity of 372 mAh g^{-1}.[5,6] Among all the available cathodes for lithium-ion batteries, $LiTMO_2$ (TM = Ni, Co, Mn or Al) (NCM or NCA) based layered oxide materials are potential candidates for high performance LIBs because of their high theoretical capacity, low cost and high operating voltage.[7] In recent years, efforts are being made to reduce the cobalt content in the layered NCM materials due to high cost, toxic nature, environmental hazards, and human rights violations in Co mining.[8–11] Moreover, reducing cobalt and increasing Ni-content in the NCM cathode is helpful in lowering the overall cost of the cathode along with increasing the energy density.[11,12] Ni-rich $Li[Ni_xCo_yMn_z]O_2$ ($x > 0.6$; $(x + y + z) = 1$) (NCM) and $Li[Ni_{1-x-y}Co_xAl_y]O_2$ (NCA), are most studied cathode materials for lithium-ion due to their potential application in next generation energy storage systems.[13] However, with increase in nickel content, these cathode materials suffer from issues such as capacity fading, poor rate capability, cyclic instability and thermal instability.[14–18] Several modification techniques such as doping, coating, morphological designs, and single crystal are employed to address the issues related to Ni-rich cathode materials to improve their electrochemical performance.[19–22] Among these mentioned modification strategies, doping or partial substitution, where a foreign metal is incorporated to stabilize the crystal lattice of Ni-rich cathodes, is now increasingly popular because of its

---

[a] *Department of Chemical and Life Science Engineering, Virginia Commonwealth University, Richmond, VA, 23219, USA. E-mail: rbgupta@vcu.edu*
[b] *Chemical Sciences Division, Oak Ridge National Laboratory, Oak Ridge, TN, 37831, USA*
[c] *Ionblox Inc., Fremont, CA, 94538, USA*

effectiveness and simplicity.[23,24] It is well known that cobalt plays an important role in the crystal structure of NCM cathode material due to its electronic configuration. Cobalt can effectively reduce the Li^+/Ni^{2+} mixing by screening the $Ni^{+2}–O_2–Ni^{+2}/Mn^{+4}$ (180°) linear interlayer super exchange interaction due to the absence of unpaired electron in its electronic configuration Co^{+3}.[25–27] However, the high cost, toxicity and socio-political issues limits the application of Co. Interestingly, Fe^{+3} has a similar electronic configuration as cobalt and can be used in NCM materials to reduce the Li^+/Ni^{2+} mixing.[27–36]

Furthermore, it is well known that the quality of precursors plays a significant role in the electrochemical performance of the cathode. Co-precipitation technique in combination of batch or semi-batch reactor is generally employed to produce the precursors for NCM cathode materials. However, the spatial inhomogeneities in batch and semi-batch reactors and variation from batch to batch hampers the quality of the product.[37,38] Therefore, continuous reactors are employed to improve the quality and increase the throughput of the product. Among continuous reactors, slug flow continuous reactors use tubes with the diameter of millimeter scale where flowing slugs of two or three different phases are used to carry out reactions. As the fluid flows in the tube maintained at the desired temperature, the reaction takes place. The homogeneity of each slug is maintained due to the intrinsic properties of slug flow which doesn't require an external agitator such as mixing blades or stir bar. Furthermore, the small microliter volume of slugs along with internal circulation enhances heat and mass transfer within the microreactor.[39–43] Three phase systems are preferred over two-phase systems as the latter suffer from injection inaccuracies and fouling due to the affinity of products towards the tube walls. In three phase systems, a carrier liquid is used to isolate the chemical reagents from the tubing walls, thus preventing fouling.[44] Mineral oil is chosen as a continuous phase which separates the solid precipitate from a direct contact with the tubing, which can help avoid clogging of the reactor tubing. The surface tension for the nitrogen–mineral oil is much lower than that of the nitrogen–water system, so nitrogen–oil interfaces are energetically preferred in the case of water–oil–nitrogen three-phase flow *i.e.*, less capillary pressure needs to be overcome. Also, the tubing material is hydrophobic. Therefore, for the water–oil–nitrogen system in this research, oil is the continuous phase, nitrogen and water are the dispersed phases.[45] The reagent addition is also improved in three phases due to a density difference between the reactants and the carrier liquid.[44]

In this work a three-phase continuous slug flow reactor is used to synthesize high quality NCMFe battery cathode precursors using coprecipitation chemistry. The effect of reagent concentration and feeding sequence on the nature of the precursor particle are evaluated first. The experimental optimized parameters are further verified with the help of mathematical modelling. Here, the cobalt is partially substituted by iron to study the effect on the electrochemical performance of $Li[Ni_{0.85}Co_{(0.1-x)}Mn_{0.05}Fe_x]O_2$ (NCMFe) (where x = 0, 0.02, 0.04). The effect of varying amount of Fe on rate capability is examined at various C-rates.

2. Experimental section

2.1. Materials

Nickel(II) sulfate hexahydrate (≥98%), manganese(II) sulfate monohydrate (≥99%), cobalt(II) sulfate heptahydrate (≥99%),

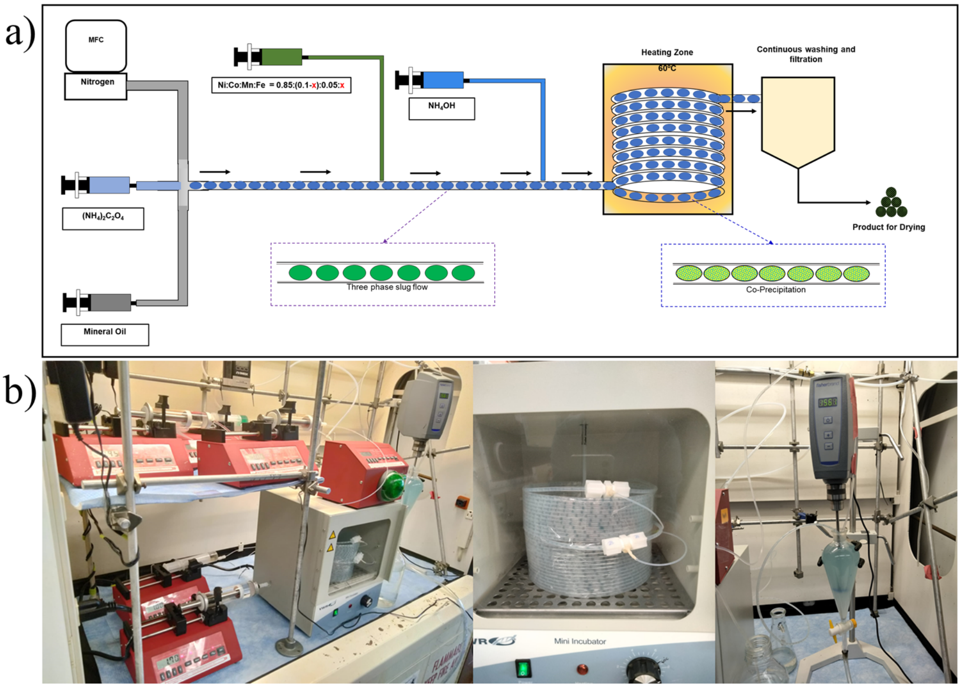

Fig. 1 (a) Schematic diagram, and (b) photograph of slug flow manufacturing platform.

ammonium oxalate monohydrate (≥99%), ammonium hydroxide (28–30% NH_3 in H_2O by weight, purity ≥99.99%), iron sulfate, light mineral oil and lithium hydroxide (≥98%) were purchased from Sigma-Aldrich. All chemicals were used as received without further treatment. All the solutions were prepared with deionized water (DI).

2.2. Slug-flow synthesis of oxalate precursors

A schematic of three phase slug flow reactor used for this work is shown in Fig. 1. The experimental setup consists of a fluorinated ethylene propylene (FEP) tube (internal diameter 2.4 mm) as a tubular reactor, four syringe pumps (New era model #1000) to inject the reagents and oil into the reactor, a mass flow controller (Omega, model# FMA-2716A) to control the gas flowrate and heating incubator. A stable three phase slug flow is generated by pumping the three phases (oil, nitrogen and reagents) into the tube with precisely controlled flowrates.[46,47] To synthesize NCMFe with different composition, stoichiometric amount of $NiSO_4{\cdot}6H_2O$, $CoSO_4{\cdot}7H_2O$, $MnSO_4{\cdot}H_2O$, and $FeSO_4{\cdot}7H_2O$ are dissolved in DI water to prepare a metal-ion solution with a 0.5 M concentration and filled into the syringe. At first T-junction, oil, nitrogen and metal salts are injected to form stable slug flow pattern. Once the flow is stabilized, NH_4OH is then injected to chelate the metals salts and increase the pH of the mixture to around 7.5. Lastly, ammonium oxalate is injected to trigger the nucleation. The slugs then pass through 50 feet of tube (equivalent to approximately 6 min of residence time) kept in a heading incubator maintained at 60 °C. As the slugs containing nuclei move downstream in the heated zone the growth of these particles takes place. The outlet of the tubular reactor, slug containing blue precipitates are collected into a 3-neck round bottom flask (with drain) containing DI water to quench and wash the solid precipitate.

2.3. Lithiation of the precursors

The solid products set at the bottom of the flask are collected, washed and filtered, followed by drying at 80 °C for 12 h to obtain the final precursor powder. The oil from the filtrate is separated and recycled. The oxalate precursor is then mixed thoroughly with $LiOH{\cdot}H_2O$ using a mortar and pestle in a molar ratio of 1 : 1.05 [(Ni + Co + Mn + Fe) : Li]. This mixture is calcined in a tube furnace at 750 °C at a ramp rate of 0.4 °C min^{-1} for 12 h in an oxygen environment. The samples are naturally cooled down to ambient before crushing them to obtain final $Li[Ni_{0.85}Co_{(0.1-x)}Mn_{0.05}Fe_x]O_2$ (where x = 0–0.04) cathode power material. The chemical reactions involved in the synthesis of the NCMFe materials are included in SI. The samples are labelled as NCMFe-(10,0), NCMFe-(8,2) and NCMFe-(6,4), based on the amount of Co and Fe in the samples.

2.4. Material characterization

The morphology and element distribution of the precursors and lithiated powders were analyzed with scanning electron microscopy (SEM, SU-700, Hitachi) equipped with energy dispersive spectroscopy (EDS) system. The crystallographic details were determined by X-ray powder diffraction (PANalytical, Empyrean X-ray diffractometer) using Cu Kα (λ = 1.5406 Å) radiation source with a step of 0.02° at 40 kV and 40 mA. Inductively coupled plasma-optical emission spectrometry (ICP-OES, Agilent Technologies, 5110-MS) was used to carry out compositional analysis of the material. X-ray photoelectron spectroscopy (XPS) of the lithiated material was performed using Phi VersaProbe III scanning XPS microprobe.

2.5. Electrochemical measurements

The electrochemical measurements were performed using CR2032 type coin cell provided by MTI. A slurry consisting of active material, conductive carbon (SuperP) and polyvinylidene difluoride (PVDF)(HSV900) in *N*-methyl pyrrolidone (NMP)(Sigma) [weight ratio of 8 : 1 : 1] is prepared by mixing these compounds at 2500 RPM for 12 min using Thinky mixture (AR-100). The resulting slurry was then coated on a battery grade aluminum foil using doctors' blade technique. The coated electrodes are then dried at 110 °C for 12 h, calendered and punched into 14-mm diameter round disc. The coin cells were assembled in an argon-filled glove box (MBraun, O_2 < 0.05 ppm and H_2O < 0.05 ppm). Celgard 2340 tri-layer microporous membrane was used as a separator and 1.0 M $LiPF_6$ in ethylene carbonate/dimethyl carbonate (EC/DMC = 1 : 1) was used as the electrolyte. Lithium metal disk was used as an anode for half-cell configuration. The loading of the electrodes was maintained at 6–8 mg cm^{-2} based on the total mass of the electrodes. The electrochemical performance of the cathode is evaluated through charge–discharge, rate capability and cycle life in MTI and ARBIN battery cycler considering 1C = 180 mA g^{-1}. The electrochemical impedance spectroscopy (EIS) was performed at various stages of cycling with an amplitude of 5 mV within a frequency range of 10^5 Hz to 10^{-2} Hz using a Gamry potentiostat Interface 5000E. All electrochemical tests were conducted at room temperature.

3. Results and discussion

3.1. Optimization of slug-flow reactor

Continuous precipitation of high-quality transition metal (TM) cathode precursor requires an optimized reactor setup. In order to find the best condition to precipitate the TM for cathode precursors, a series of controlled experiments were conducted in terms of feeding sequence, feeding location, flowrates and concentration of the reagents. In this section, effects of each of these conditions are studied to optimize the synthesis parameters for slug-flow reactor.

3.1.1. Effect of chelating/precipitating agent concentration on the precursor particle

(i) Concentration of $(NH_4)_2C_2O_4$ solution. Ammonium oxalate ($(NH_4)_2C_2O_4$) plays the role of chelating as well as precipitating agent.[48] Due to its solubility constrain, the maximum concentration of ammonium oxalate cannot be over 0.3 M at 25 °C. When the concentration of ammonium oxalate is changed from 0.15 M to 0.255 M, keeping metal-ion and ammonium hydroxide as 0.5 M each, the yield decreased due to the presence of

insufficient amount of $C_2O_4^{-2}$ (at 0.15 M) to precipitate out all metal ion solution. The optimum concentration of ammonium oxalate is established as 0.255 M to achieve a high yield.

(ii) Concentration of NH_4OH solution. Ammonium hydroxide (NH_4OH) is a chelating agent and pH regulator for the precipitation reaction. It binds with metal ions to form metal amine complexes and releases them slowly with an increase in pH.[48] In this control experiment, the concentration of metal ions and ammonium oxalate is kept constant at 0.5 M and 0.255 M, respectively, while the ammonium hydroxide is varied from 0.1 to 2 M. When the concentration of ammonium hydroxide is at 0.1 M, cuboidal particles are formed along with some small primary particles attached to them due to a slight chelation of metal ions as shown in Fig. S1a. With the increase in the concentration of ammonium hydroxide, the formation of amine complexes increases, and primary particles size reduces. On the other hand, if the concentration of ammonium

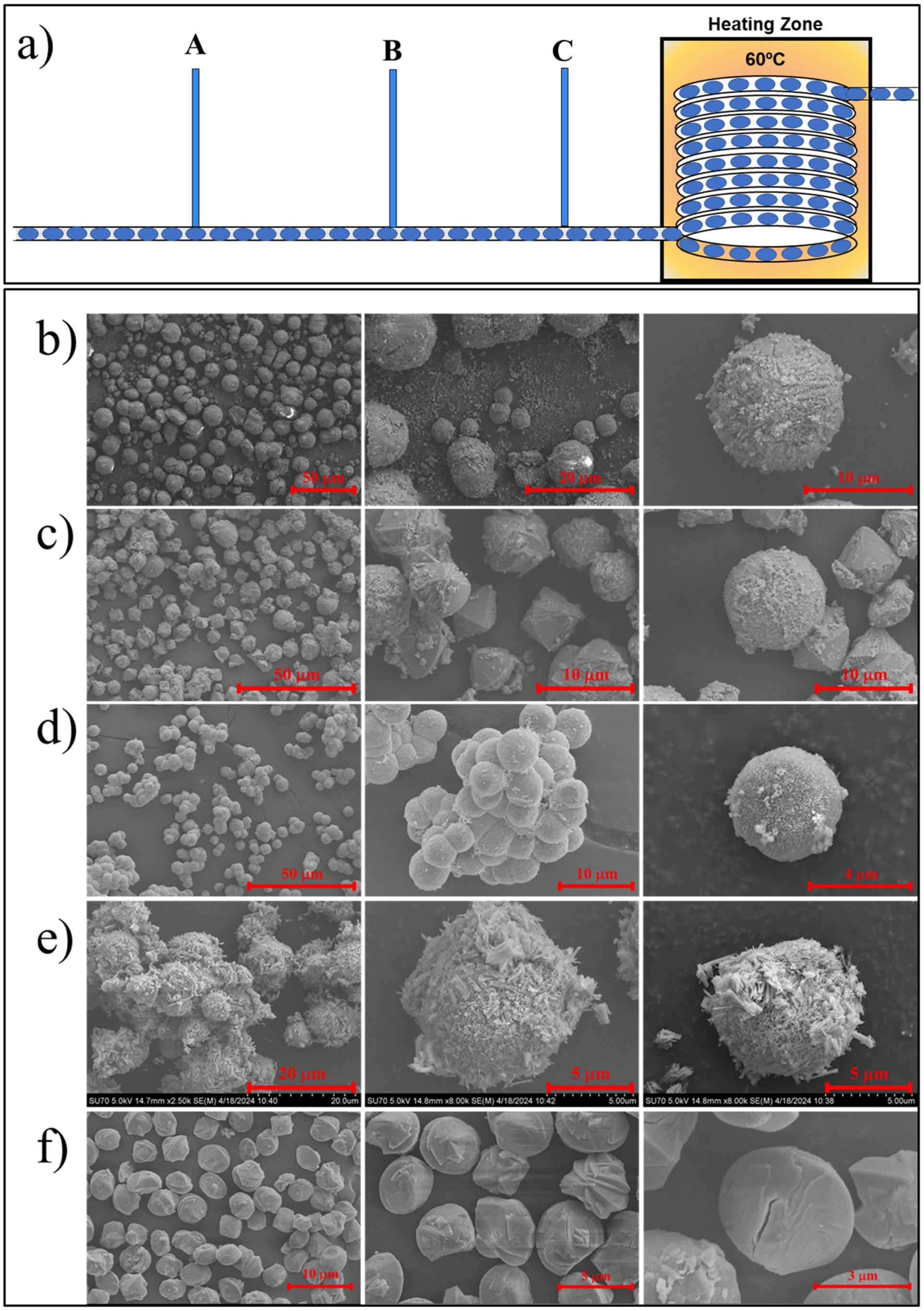

Fig. 2 (a) Schematic of the slug-flow with the feeding points of reactant solutions. Scanning electron microscopy of oxalate precursors derived from different feeding sequences: (b) sequence (i), (c) sequence (ii), (d) sequence (iii), (e) sequence (iv), and (f) sequence (v), as described in the Section 3.1.2.

hydroxide is increased to 2.0 M, metal-ion partially precipitates out as hydroxide and secondary particles grow bigger along with hydroxide primary particles attached to them (Fig. S1e). The optimum ammonium hydroxide is obtained as 0.5 M where the primary particles are all agglomerated and well packed to form the secondary particles and there is minimum formation of metal hydroxides (Fig. S1c).

These findings highlight that both the concentration of ammonium oxalate and ammonium hydroxide significantly influence the yield and morphology of the precipitated precursor. An optimal concentration of 0.255 M ammonium oxalate ensures sufficient oxalate ions for complete precipitation, while 0.5 M ammonium hydroxide promotes controlled complexation and uniform secondary particle formation. Deviations from these concentrations result in either incomplete precipitation or formation of undesired hydroxide phases, underscoring the importance of fine-tuning reagent concentrations for high-quality precursor synthesis in slug-flow reactors.

3.1.2. Effect of feeding sequence.

Nucleation and growth of the precursor particles can be controlled by adding the reagent in a specific order, thus dictating the final particle morphology and composition. To study the effect of feeding sequence of reagents on the morphology of the secondary particle, controlled experiments are carried out using different combinations of feeding sequence. Fig. 2a shows the locations where these reagents are added. For sequence optimization, the reactant concentrations are kept at: 0.5 M metal-ion, 0.255 M $(NH_4)_2C_2O_4$, and 0.5 M NH_4OH.

(i) A = metal-ion; B = NH_4OH; C = $(NH_4)_2C_2O_4$. Ammonium hydroxide plays a role of chelating agent and a pH regulator in the co-precipitation of metal salts. In this sequence, ammonium hydroxide is injected after metal-ion to form metal-amine complexes. The formed complexes then travel downstream where $(NH_4)_2C_2O_4$ is added to trigger the precipitation. The morphology and particle sizes are found to be random in this case (Fig. 2b). Here, $FeSO_4$ is transformed into amorphous iron hydroxide as soon as it came into contact of NH_4OH and thus separated out from rest of the metal amine complex. This causes severe inhomogeneity in particle size, morphology, and composition of the product.

(ii) A = metal salts; B = $(NH_4)_2C_2O_4$; C = NH_4OH. When the ammonium oxalate is injected into metal-ion before ammonium hydroxide, some of the metals precipitate as metal oxalate at room temperature before reaching to ammonium hydroxide injection point. This partial precipitation of metals results in a mixed morphology of cuboidal and spherical (Fig. 2c).

(iii) A = $(NH_4)_2C_2O_4$; B = metal salts; C = NH_4OH. Iron sulfate precipitates as hydroxide and form separate particles which can lead to an inaccurate composition of final material in case (i). Thus, to prevent the precipitation of iron, this sequence was tested. Moreover, the stoichiometric volume of 0.255 M ammonium oxalate required to precipitate a 50 mL, 0.5 M metal sulphate solution is approximately 98 mL. Therefore, the flowrate of $(NH_4)_2C_2O_4$ is highest among the three reactants. For a stable flow system, it is better to have a high flowrate solution at starting so that the terminal velocity of the system is constant throughout the reactor. In this scenario, the particles formed are spherical with a narrow particle size distribution (Fig. 2d).

(iv) A = $FeSO_4$ + $(NH_4)_2C_2O_4$; B = Ni, Co and Mn sulfate solution; C = NH_4OH. Iron sulphate tends to form iron hydroxide when dissolved in DI water. This causes the iron to precipitate inside the syringe during the course of injection. To avoid this, the iron sulphate is dissolved in ammonium oxalate solution as it is slightly acidic and can keep iron in the solution form. The results from this experiment show that the final morphology of the secondary particles is spherical, but some part of primary particles do not agglomerate together to form secondary particles Fig. (2e).

(v) A = metal salts; B = $(NH_4)_2C_2O_4$. When only metal and ammonium oxalate are used, the morphology of the precursor materials is cuboidal. This happens due to the absence of a chelating agent which forms a complex with metal-ions and slowly releases them to form smaller primary particles. These primary particles then agglomerate to form spherical secondary particles. When there is no chelating agent, the metal ion precipitates rapidly and forms cuboidal particles (Fig. 2f).

In summary, the feeding sequence of reagents has a strong effect on the particle morphology, size distribution, and composition of the cathode precursors. When ammonium hydroxide is added first, iron precipitates as hydroxide, leading to irregular shapes and non-uniform composition. Injecting ammonium oxalate before the metal salts results in better control over nucleation and growth. Among all the sequences tested, the most uniform and spherical particles with narrow size distribution are obtained when ammonium oxalate is introduced first, followed by metal salts, and then ammonium hydroxide. This sequence ensures stable flow conditions and minimizes unwanted side reactions (hydroxide formation), leading to consistent precursor quality.

3.2. Mathematical modelling of co-precipitation in slug-flow reactor

Equilibrium modeling techniques developed for various formulations of NCM hydroxide and NCM oxalate are modified and applied to NCMF oxalate experiments to explore the effect of changing concentrations of inputs in the region about a central case (Table 1).[49] The solution equilibrium model finds the equilibrium concentrations and amounts of components in the NCMFe oxalate system co-precipitation reaction by solving a system of balances and chemical reaction equilibria. The overall mass balance within each slug, assuming the volumes are additive, is given as:

$$V_T = V_1 + V_2 + V_3 \quad (1)$$

where V_T is the total volume and V_1, V_2 and V_3 correspond to the volume of metal sulfate, $(NH_4)_2C_2O_4$ and NH_4OH solutions. The

Table 1 The experimental inputs for the precipitation of NCMF oxalate used as the central case for an exploratory model provide a weakly basic solution (pH ≈ 8) and a 2% excess of oxalate

Input	Concentration (M)	Flowrate (mL min^{-1})
Metal sulfate	0.5	0.50
(85% Ni, 10% Co, 5% Mn, 0% Fe)		
(85% Ni, 8% Co, 5% Mn, 2% Fe)		
(85% Ni, 6% Co, 5% Mn, 4% Fe)		
Ammonium oxalate	0.3	0.85
Ammonium hydroxide	0.4	0.50

mass balances for the total concentration of each of the three metal ions, oxalate ions and ammonia in solution are shown in eqn (2)–(4) respectively.

$$p_{\mathrm{M}}[\mathrm{MSO_4}]_{\mathrm{in}}V_1 = \left([\mathrm{M}^{2+}] + \sum[\mathrm{M(C_2O_4)}_i] + \sum[\mathrm{M(NH_3)}_i]\right)V_{\mathrm{T}} + n_{\mathrm{MOx(s)}} \tag{2}$$

$$[(\mathrm{NH_4})_2\mathrm{C_2O_4}]_{\mathrm{in}}V_2 = \left([\mathrm{C_2O_4}^{2-}] + [\mathrm{H_2C_2O_4}]\right)V_{\mathrm{T}} + \sum n_{\mathrm{MOx(s)}} + \sum i[\mathrm{M(C_2O_4)}_i] \tag{3}$$

$$2[(\mathrm{NH_4})_2\mathrm{C_2O_4}]_{\mathrm{in}}V_2 + [\mathrm{NH_4OH}]_{\mathrm{in}}V_3 = [\mathrm{NH_3}] + [\mathrm{NH_4}^+] + \sum i[\mathrm{M(NH_3)}_i] \tag{4}$$

where p_{M} is the molar ratio of transition metal (M), M refers to the individual transition metals, *i.e.* Ni, Co, Mn, and Fe. The input concentrations on the left-hand side of eqn (2)–(4) are also known. The remaining concentrations and amounts are determined by the equilibrium equations for metal oxalate, water, ammonium hydroxide, and metal-amine or metal-oxalate complexes. The details of equations and hypothesis used for theoretical modelling are included in SI (Tables S1–S4). The outcome of the modelling analysis is shown in Fig. 3 and Fig. S2.

3.2.1. Effect of changing the concentration of $(\mathrm{NH_4})_2\mathrm{C_2O_4}$. In increments of 0.01 M, the first factor investigated was the input concentration of ammonium oxalate (Fig. 3a). The maximum overall amount of oxalate precipitate produced is seen to occur at or about the central case, while the yield of individual components of cobalt and manganese are maximized for ammonium oxalate concentration less than 0.3 M, and iron and nickel are maximized for ammonium oxalate concentration greater than 0.3 M. All four metals decrease in yield with insufficient ammonium oxalate, but the greatest relative effect is seen for iron; there exists a threshold below which virtually no iron oxalate precipitates, at 0.25 M ammonium oxalate for the case of 2% iron and 0.22 M ammonium oxalate for 4% iron. Starting from the case of oxalate deficiency (on the left of each subplot), adding oxalate (moving right) increases the amount of product (with a maximum of 0.025 mole due to metal as the limiting reactant) subject to the limit dictated by the solubility product constant; however, there comes a point beyond which the additional ammonium ions being added simultaneously creates a solution with a greater affinity for metal ions in the form of ammine complexes, thus overcoming the benefit of added oxalate. As seen in Fig. 3a, cobalt and manganese ions have the highest sensitivity to the inherent tradeoff.

3.2.2. Effect of changing metal sulfate concentration. Next, investigating the effect of changing the input concentration of the metal sulfates, while maintaining the specified ratio (*i.e.*, NCMF = 0.85, 0.1–x, 0.05, x), one can again observe the increase in product starting from a state of deficiency and increasing this time, the amount of metal available (Fig. 3b). There is no intermediate maximum amount of product in this case, because there is no significant simultaneous change in solution chemistry due to the increased sulfate (as seen with the ammonia above). The maximum possible amount produced now is dictated by the limiting reactant, oxalate (max = 0.0255 M). Near the central case, iron has displaced cobalt as designed, but as more cobalt becomes available; while maintaining constant oxalate, cobalt oxalate is seen to be the preferred precipitate over iron oxalate, in agreement with the solubility product constants.

3.2.3. Effects on precipitate of changing the concentration of $\mathrm{NH_4OH}$. The observation of the effects of changing the input concentration of ammonium hydroxide is consistent with the previous discussion (Fig. 3c); *i.e.*, as more ammonia is added to the system, more metal ion can be held in solution at equilibrium in ammine complexes. As a result, less overall precipitate is produced. The concavity of the trends in yield for the individual components differs for iron compared to the other three metals, consistent with iron being less amenable to forming amine complexes at the given concentrations, so iron oxalate production remains relatively stable, while the nickel, cobalt, and manganese oxalate formation decreases more precipitously.

The model confirms that the oxalate concentration strongly influences the yield, with an optimal value around the central case. Iron precipitation is particularly sensitive to oxalate deficiency, while excessive oxalate and ammonium ions can reduce yields by promoting ammine complex formation. Increasing metal sulfate concentration improves yield up to the oxalate-limited threshold, with cobalt preferentially precipitating over iron under excess metal conditions. Lastly, higher ammonium hydroxide concentrations lead to lower yields due to the formation of soluble ammine complexes, especially for nickel, cobalt, and manganese. These findings guide precise control of precursor composition and yield in multi-component co-precipitation systems.

The optimization of the slug-flow reactor focused on identifying key process parameters for the controlled co-precipitation of NCMF oxalate precursors. Experimental results demonstrated that a concentration of 0.255 M ammonium oxalate and 0.5 M ammonium hydroxide provided optimal conditions for high yield and uniform particle morphology. The feeding sequence was also found to be critical. Introducing ammonium oxalate before the metal sulfate solution, followed by ammonium hydroxide, produced spherical secondary particles with consistent size and composition. This sequence prevented

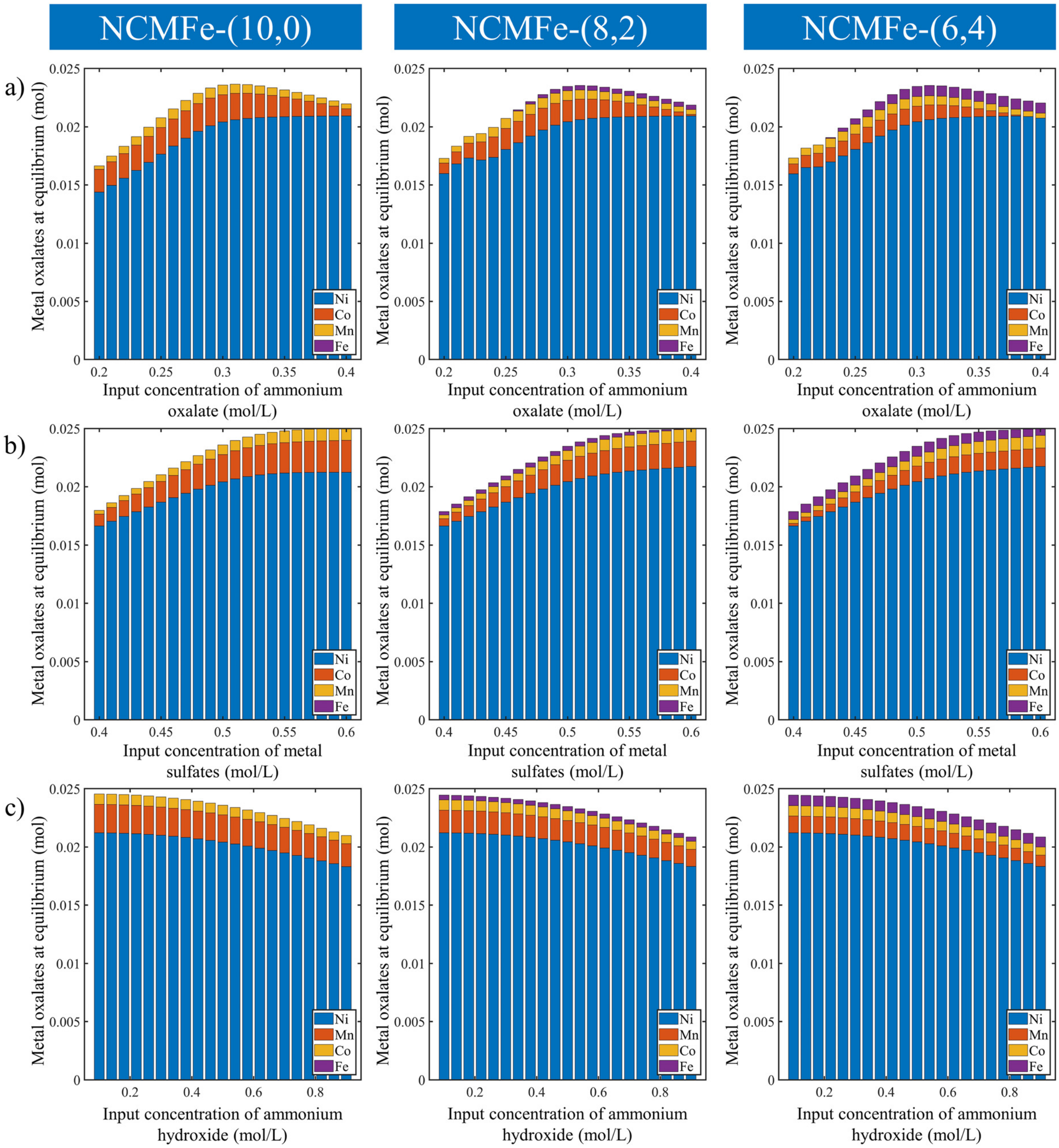

Fig. 3 The effect on precursor yield and composition as a result of changing the input concentration of (a) ammonium oxalate, (b) metal sulfates, and (c) ammonium hydroxide, for NCMFe-(10,0), (8,2) and (6,4).

premature iron hydroxide formation and ensured better control over nucleation and growth. Additionally, to further understand the precipitation behavior, a solution equilibrium model was developed and applied to the NCMF oxalate system. The model incorporated mass balances and equilibrium reactions to evaluate how changes in input concentrations of ammonium oxalate, ammonium hydroxide, and transition metal sulfates influence precipitation. Modeling results aligned with experimental trends, indicating that iron precipitation is highly sensitive to oxalate availability, while excess ammonium hydroxide reduces overall precipitation through metal-ammine complex formation. Cobalt was found to preferentially precipitate over iron when oxalate is limited, consistent with differences in solubility product constants. These findings offer a validated framework for optimizing continuous co-precipitation in multicomponent cathode systems.

3.3. Characterization of NCMFe samples

Fig. 4a–c shows the SEM images of lithiated cathode materials at different magnifications. It is observed that a slow ramp rate during lithiation step (decomposition of oxalate to oxide) helps in retaining the spherical morphology of the final oxide materials with an average particle size of 2–5 μm and the Fe-content does not affect the particle size of the material. The EDAX maps of the three samples are shown in Fig. 4d, showing a homogeneous distribution of all the metals ions. The chemical composition of the three samples is confirmed using ICP-OES, shown in Fig. S3, indicating that the Fe is successfully incorporated into NCM materials.

The X-ray diffraction pattern for lithiated NCMFe-(10,0), (6,4) and 8,2) materials are shown in Fig. 5(a). The observed spectra for all three samples can be indexed to layered hexagonal α-$NaFeO_2$ structure with $R\bar{3}m$ space group. The magnified reflections (003) and (104) peaks are shown in Fig. 5(b) and (c) which shows the effect of incorporation of iron into the sample. It is observed that as the iron content increases from 0% to 4%, both the reflections shift towards lower 2θ values. This indicates an increase in interplanar distance in iron containing samples due to a larger ionic radius of Fe^{+3} (0.65 Å) compared to Co^{+3} (0.55 Å), which in turn is known to improve the Li^+ ion diffusion in the layered structure leading to an enhanced rate capability of material.[34] Rietveld refinement is performed to further analyze the XRD data, Table 2 shows the calculated lattice parameters for three samples. The intensity ratio I_{003}/I_{104} remains almost similar as the iron content is increased from 0% to 2% while decreasing the cobalt content from 10% to 8%, indicating a similar extent of Li^+/Ni^+ mixing in both the samples. On the contrary, a lower intensity ratio for NCMFe-(6,4) indicates a high degree of mixing. The c/a ration for all three materials is greater than 4.94 which indicates the formation of a well-defined hexagonal crystal structure. The splitting of (006)/(012) and (108)/(110) peaks confirm the formation of layered structure.[50] It is observed from the Rietveld refinement that there is an increase in the lattice volume with an increase in the iron content in the samples.

XPS analysis is used to further understand the oxidation states of different elements in the oxide samples. The survey scan for NCMFe is included in SI (Fig. S4). The high-resolution Ni $2p_{3/2}$ and Mn $2p_{3/2}$ for all the three samples, such as NCMFe-(10,0), (8,2) and (6,4) are included in Fig. 6 to show the effect of Fe^{3+} doping. In all the cases, the Ni $2p_{3/2}$ peaks are observed at 855.05 eV with a satellite peak at 861.25 eV. The $2p_{3/2}$ can be deconvoluted in two peaks at 854 and 856 eV, corresponding to the Ni^{2+} and Ni^{3+}, respectively. From Fig. 6a, c and e it is observed that the Ni^{3+} content is increasing with the increasing amount of Fe^{3+}. The deconvoluted Mn $2p_{3/2}$ spectra for all the three samples are shown in Fig. 6b, d and f. Mn 2p3/2 is observed at 642 eV and it is deconvoluted into two distinct peaks, indicating the presence of Mn^{3+} and Mn^{4+} states. In this case also, Mn^{4+} is found to be increased compared to Mn^{3+} with the increasing amount of Fe^{3+}. For all the three cases, the high-resolution Co $2p_{3/2}$ peak is observed at 779 eV, which is primarily composed of only +3 oxidation state (Fig. S5a–c). The Fe $2p_{3/2}$ spectra for both the NCMFe-(8,2) and NCMFe-(6,4) primarily contains the +3 peak at 712 eV (Fig. S5d and e).

3.4. Electrochemical performance

The electrochemical studies were performed on three samples using CR2032 type coin cell with Li-foil (half-cell) as anode. All experiments were performed at room temperature and within a voltage window of 2.8–4.3 V *vs.* Li/Li^+. The initial charge–discharge at 0.1C for all three materials is shown in Fig. 7a, the discharge capacity of NCMFe-(10,0), (8,2), and (6,4) are 200.6, 172.5 and 173.2 mAh g^{-1}, respectively. It is observed that the specific capacity decreases with an increase in iron content. To study the long-term performance, cycling stability test is conducted on three samples for 100 cycles at 0.5C within a voltage window of 2.8–4.3 V in half cell (Fig. 7b). The percentage of capacity retained by each sample after 100 cycles is 53%, 47% and 39% for NCMFe-(10,0),NCMFe-(8,2) and NCMFe-(6,4), respectively. The reason for low coulombic efficiency in the case of NCMFe-(6,4) can be attributed to the local distortion of the structure due to a phase change from hexagonal to cubic. It is observed that with the increase in the Fe-content in the NCM structure some of the Fe stabilizes in the lithium layer (3a) instead of TM-layer (3b), which hinders the lithium diffusion back into the cathode.[51,52] The cycling performance of both the iron containing sample is poorer than the undoped-NCM sample due to the local phase changes and distortion. The charge–discharge analysis for all the three materials is performed within a wide range of C-rates, ranging from 0.1C to 2C (Fig. S6). The rate capability plot for three samples at different C-rates is shown in Fig. 7c. It is observed that at low C-rates, up to 0.5C, the sample without iron performs better compared to samples with iron. However, when the C-rate is increased above 0.5C, it is seen that NCMFe-(8,2)

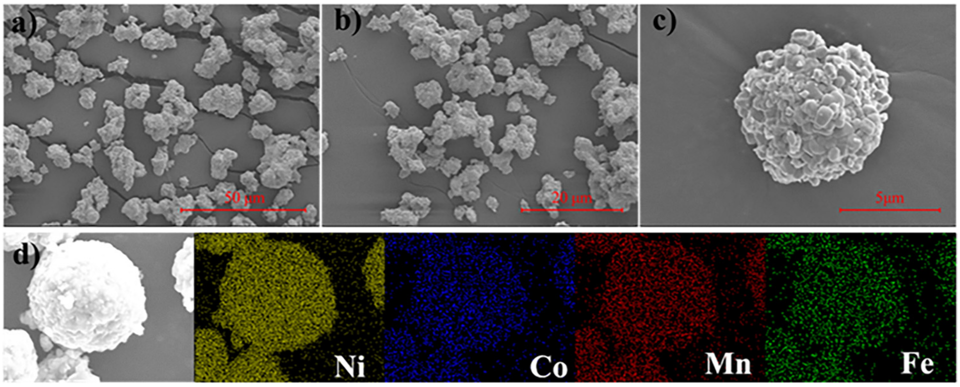

Fig. 4 (a)–(c) SEM images and (d) EDAX mapping of NCMFe-(8,2).

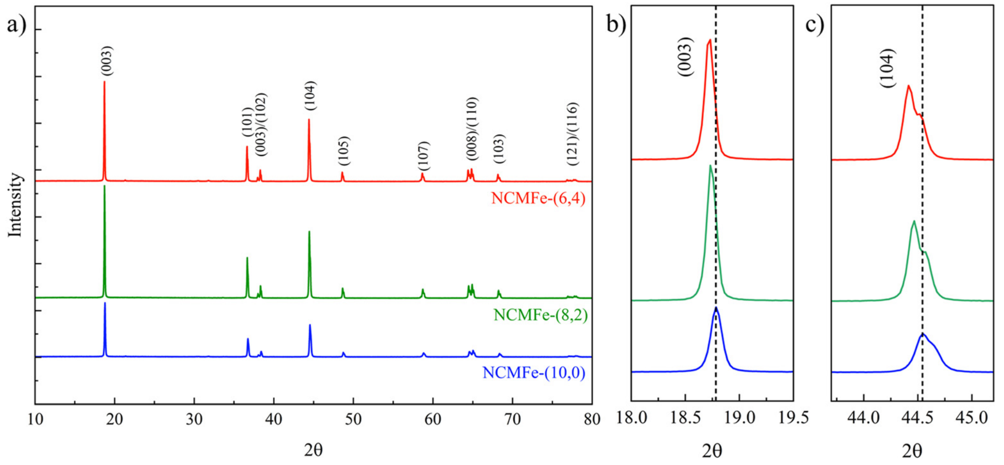

Fig. 5 (a) XRD profiles, (b) (003)-shift and (c) (104)-shift of NCMFe-(10,0), (8,2) and (6,4).

Table 2 Refinement data of the XRD profiles of three NCMFe cathodes

Sample	*a* & *b* (Å)	*c* (Å)	*V* (Å^3)	*c*/*a*	$I_{(003)}/I_{(104)}$
NCMFe-(10,0)	2.86566	14.1728	100.8134	4.94574	1.67
NCMFe-(8,2)	2.86937	14.1878	101.1629	4.94452	1.68
NCMFe-(6,4)	2.87207	14.1997	101.4382	4.94406	1.60

shows a better charge storage performance compared to NCMFe-(10,0) and NCMFe-(6,4), with latter performing the worst at higher C-rates. Here, it is observed that the rate capability of NCMFe-(8,2) is better than the other two materials at 2C, retaining 70% of its capacity at 0.1C. Whereas NCMFe-(10,0) and NCMFe-(6,4) samples retained 34% and 24%, respectively. Furthermore, when the current rate was changed back to 0.1C, NCMFe-(8,2) regains 97% of its initial capacity (at 0.1C) while NCMFe-(10,0) regains 92% of its initial capacity. On the other hand, NCMF-(6,4) only regains 44% of its capacity at 0.1C, indicating severe degradation of materials due to higher charging and discharging currents. The poor rate capability of the NCMFe-(6,4) is attributed to the irreversible phase change from hexagonal to cubic structure due to the presence of Fe in the Li (3a) layer.[52–54]

In order to understand the effect of Fe^{3+}-content on the rate capability the deferential capacity (d*Q*/d*V* *versus* *V*) plots are

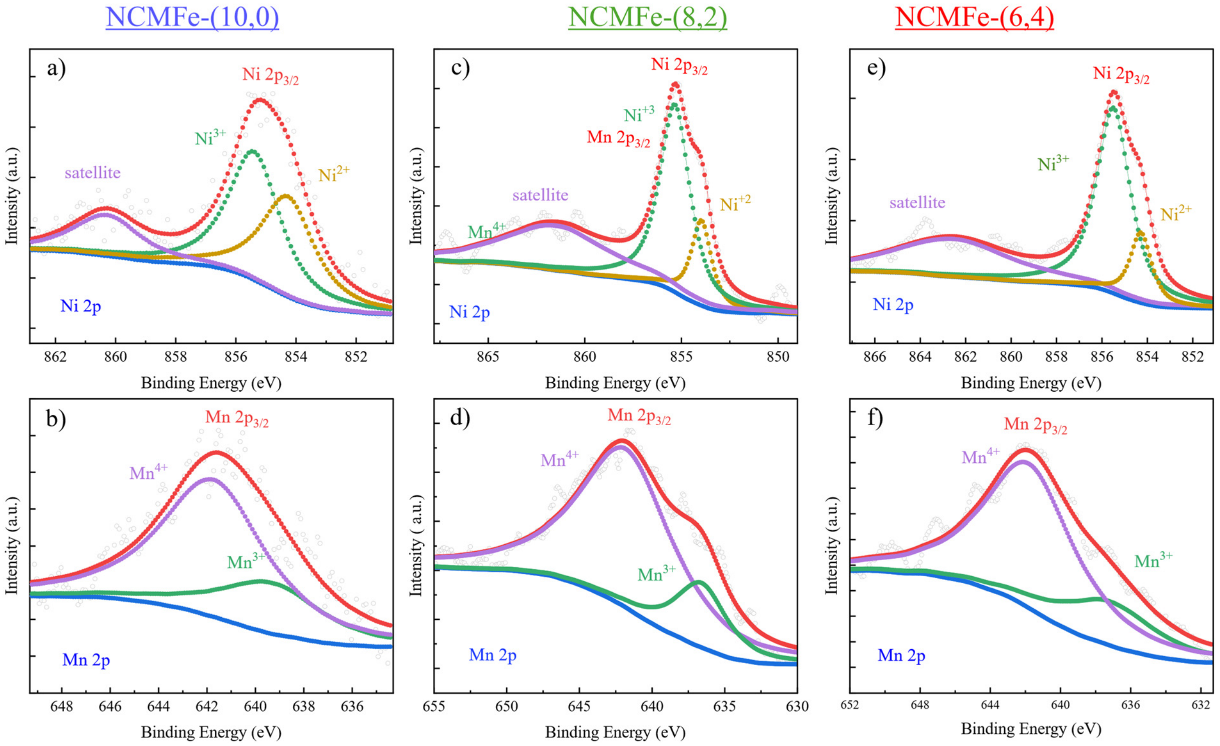

Fig. 6 High-resolution XPS Ni 2p and Mn 2p profiles for (a) and (b) NCMFe-(10,0), (c) and (d) NCMFe-(8,2) and (e) and (f) NCMFe-(6,4).

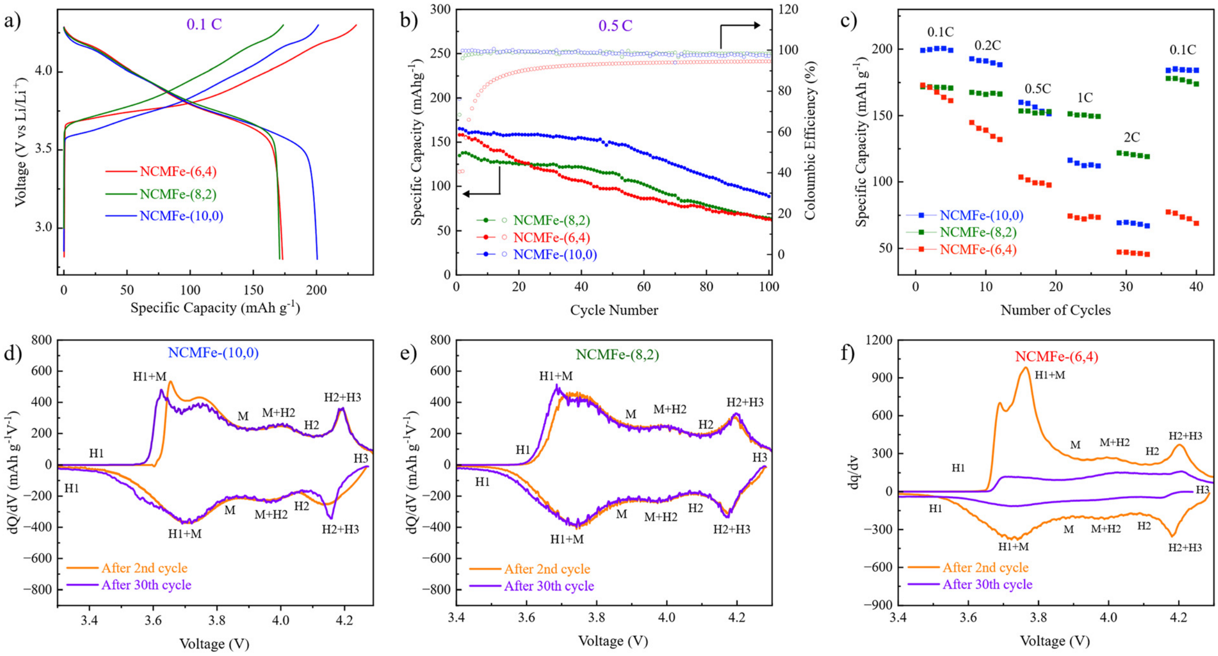

Fig. 7 Comparison of electrochemical performance of NCMFe-(10,0), NCMFe-(8,2) and NCMFe-(6,4), in terms of (a) charge–discharge at 0.1C; (b) cycling performance at 0.5C, and (c) rate capability. The differential capacity(dQ/dV) profiles of (d) NCMFe-(10,0), (e) NCMFe-(8,2) and (f) NCMFe-(6,4).

derived at the beginning and end of the rate performance (Fig. 7d–f). It is observed that the original layered hexagonal structure (H1) of the Ni-rich cathodes are first transformed to monoclinic (M) phase followed by transformation to hexagonal 1 and 2 (H1 and H2) phases upon sweeping the voltage from 2.8 to 4.3 during charging due to delithiation and the reverse phase transition happens upon lithiation during discharging.[55] Although this phenomenon is common for all three as-synthesized material, the extent of polarization in terms of peak shift and intensity variation are significantly different at the beginning from that at the end of the rate-capability experiment. Among the three, the NCMFe-(8,2) shows the least peaks shift and intensity variation, signifying a better structural stability even at higher C-rates (Fig. 7e). Whereas, NCMFe-(10,0) shows a significant change in peak intensity at the high voltage region during lithiation process (Fig. 7d). The NCMFe-(6,4) shows a significant deviation in peak structure and position at the end of rate capability experiment, which further supports its worst rate performance (Fig. 7f). Hence, from this observation it can be inferred that an optimum amount of iron doping can efficiently mitigate the phase change related issue even at higher C-rate and assure a good rate performance. In order to get a better understanding on the effect of gradual replacement of Co^{3+} with Fe^{3+} on the redox process of the Ni-rich layered cathode, electrochemical impedance spectroscopy (EIS) was performed with each of the cathodes after 10 charge–discharge cycles. After analyzing the Nyquist plots (Fig. S7a) with the help of suitable equivalent circuit (Fig. S7b), it is observed that, the electrode–electrolyte interfacial resistance (R_f) decreases with increasing amount of Fe^{3+}, signifying the improved surface conductivity. On the other hand, NCMFe-(8,2) shows the lowest charge transfer resistance (R_{ct}) compared to the other two cathodes. Furthermore, It is observed that the NCMFe-(8,2) achieves a higher Li^+ diffusion co-efficient among the three, which further signifies that an optimum doping of Fe^{3+} facilitates the diffusion throughout the crystal structure of the Ni-rich layered cathode as shown in inset of Fig. S7. This clearly indicates that a facile charge-transfer is only possible with optimum amount of Fe^{3+} doping and higher amount of doping may worsen the scenario. Hence, from the study it is observed that $Li[Ni_{0.85}Co_{(0.1-x)}Mn_{0.05}Fe_x]O_2$ with 2% Fe^{3+} and 8% Co^{3+} shows a good rate performance with a fast charge-transfer kinetics.

4. Conclusion

In this study, a slug flow continuous reactor-based on co-precipitation reactor is used to synthesize Fe^{3+} substituted Ni-rich NCM precursor for lithium-ion battery precursors with varying Co and Fe contents. The optimized reagent concentration and feeding sequence results in a high-quality spherical precursor particle with a narrow particle size distribution. After a detailed study on the effect of feeding sequence on the quality of precursor particle, an optimum condition is established to produce the spherical NCMFe-oxalate precursor of particle size of 5–7 μm. The effect of the concentrations of metal salt, ammonium oxalate, and ammonium hydroxide solutions, used for the production of NCMFe-oxalate precursors are further verified with the help of equilibrium modelling. From the modelling analysis it is also supported that the reagent concentrations used for the manufacturing process offer the highest yield and the targeted composition of the precursors. Subsequently, all the three precursors are calcinated in pre-optimized condition to produce the final layered oxide and further characterized with various physical characterization techniques, including XRD, SEM, and XPS. A detailed electrochemical performance analysis was performed with all three materials to evaluate the effect of the Co^{3+}-substitution with Fe^{3+} on the cathode performance. Here, it is observed that at low C-rates ($<0.5C$) the specific capacity of the Ni-rich cathode decreases with an increasing Fe^{3+}-content. A very high Fe^{3+}-doping (4%) results in severe degradation due to irreversible phase change. At the high C-rates of 1C and 2C, the material with 2% Fe^{3+} [NCMFe-(8,2)] shows a high specific capacity and better rate capability. Similarly, the charge transfer resistance and the polarization of electrode is the lowest for the [NCMFe-(8,2)] and offers a good rate performance.

Author contributions

Arjun Patel: material synthesis, electrochemical investigation, scientific conceptualization, Michael L. Rasche: theoretical modelling of the precursors, Sourav Mallick: electrochemistry analysis and mechanism, Sunuk Kim: slug-flow reactor discussions, Mariappan Parans Paranthaman: experimental design and revision, Herman Lopez: experimental design. Mo Jiang and Ram B. Gupta: conceptualization, supervision, and funding-acquisition. All authors contributed to and approved the final version of the manuscript.

Conflicts of interest

The authors declare no competing financial interest.

Data availability

The data supporting this article has been included as part of the SI. The supporting information include the copercipitation reactions, SEM images for different ammonium hydroxide concentration, equations and hypothesis for theoritical modelling, modelling data, ICP results, supplementary XPS data, electrochemical charge discharge and EIS plots. See DOI: https://doi.org/10.1039/d5ya00032g.

Acknowledgements

This material is based upon work supported by Virginia Commonwealth University, National Science Foundation (Grant No. CMMI-1940948) and U.S. Department of Energy, Office of Energy Efficiency and Renewable Energy, Advanced Materials and Manufacturing Technologies Office (award DE-EE0009110). Research conducted at ORNL was supported by the U.S. Department of Energy, Office of Science, Basic Energy Sciences, Materials Sciences and Engineering Division. This manuscript has been authored by UTBattelle, LLC, under Contract No. DEAC05-00OR22725 with the U.S. Department of Energy. The U.S. Government retains and the publisher, by accepting the article for publication, acknowledges that the U.S. Government retains a nonexclusive, paid-up, irrevocable, worldwide license to publish or reproduce the published form of this manuscript, or allow others to do so, for U.S. Government purposes. The Department of Energy will provide public access to these results of federally sponsored research in accordance with the DOE Public Access Plan (https://energy.gov/downloads/doe-public-access-plan). Mingyao Mou and Sophie Kothie are acknowledged for providing the slug flow co-precipitation technology developed in Mo Jiang Lab.

References

1 J. B. Goodenough and K.-S. Park, *J. Am. Chem. Soc.*, 2013, **135**, 1167–1176.

2 K. Mizushima, P. C. Jones, P. J. Wiseman and J. B. Goodenough, *Mater. Res. Bull.*, 1980, **15**, 783–789.

3 The Nobel Prize in Chemistry 2019. NobelPrize.org. Nobel Prize Outreach AB 2023. Tue. 6 Jun 2023. https://www.nobelprize.org/prizes/chemistry/2019/summary/.

4 M. Bianchini, M. Roca-Ayats, P. Hartmann, T. Brezesinski and J. Janek, *Angew. Chem., Int. Ed.*, 2019, **58**, 10434–10458.

5 W. Yan, X. Jia, S. Yang, Y. Huang, Y. Yang and G. Yuan, *J. Electrochem. Soc.*, 2020, **167**, 120514.

6 G. Bhutada, Breaking Down the Cost of an EV Battery Cell, https://www.visualcapitalist.com/breaking-down-the-cost-of-an-ev-battery-cell/, (accessed 6 February 2025).

7 S. Mallick, A. Patel, X. G. Sun, M. P. Paranthaman, M. Mou, J. H. Mugumya, M. Jiang, M. L. Rasche, H. Lopez and R. B. Gupta, *J. Mater. Chem. A*, 2023, **11**, 3789–3821.

8 Y. Lv, S. Huang, Y. Zhao, S. Roy, X. Lu, Y. Hou and J. Zhang, *Appl. Energy*, 2022, **305**, 117849.

9 F. Schipper, E. M. Erickson, C. Erk, J.-Y. Shin, F. F. Chesneau and D. Aurbach, *J. Electrochem. Soc.*, 2017, **164**, A6220–A6228.

10 N. Muralidharan, E. C. Self, M. Dixit, Z. Du, R. Essehli, R. Amin, J. Nanda and I. Belharouak, *Adv. Energy Mater.*, 2022, **12**, 2103050.

11 S. Mallick, A. Patel, M. P. Paranthaman, J. H. Mugumya, S. Kim, M. L. Rasche, M. Jiang, H. Lopez and R. B. Gupta, *Sustain. Energy Fuels*, 2025, **9**, 724–738.

12 H.-J. Noh, S. Youn, C. S. Yoon and Y.-K. Sun, *J. Power Sources*, 2013, **233**, 121–130.

13 A. Manthiram and J. B. Goodenough, *Nat. Energy*, 2021, **6**, 323.

14 H.-H. Ryu, K.-J. Park, C. S. Yoon and Y.-K. Sun, *Chem. Mater.*, 2018, **30**, 1155–1163.

15 S. S. Zhang, *Energy Storage Mater.*, 2020, **24**, 247–254.

16 G. L. Xu, X. Liu, A. Daali, R. Amine, Z. Chen and K. Amine, *Adv. Funct. Mater.*, 2020, **30**, 2004748.

17 R. Pan, E. Jo, Z. Cui and A. Manthiram, *Adv. Funct. Mater.*, 2023, **33**, 2211461.

18 Y. Gao, X. Wang, J. Geng, F. Liang, M. Chen and Z. Zou, *J. Electron. Mater.*, 2023, **52**, 72–95.

19 H. H. Sun, U. H. Kim, J. H. Park, S. W. Park, D. H. Seo, A. Heller, C. B. Mullins, C. S. Yoon and Y. K. Sun, *Nat. Commun.*, 2021, **12**, 6552.

20 J. Jeyakumar, Y. S. Wu, S. H. Wu, R. Jose and C. C. Yang, *ACS Appl. Energy Mater.*, 2022, **5**, 4796–4807.

21 U. H. Kim, H. H. Ryu, J. H. Kim, R. Mücke, P. Kaghazchi, C. S. Yoon and Y. K. Sun, *Adv. Energy Mater.*, 2019, **9**, 1803902.

22 G. Ko, S. Jeong, S. Park, J. Lee, S. Kim, Y. Shin, W. Kim and K. Kwon, *Energy Storage Mater.*, 2023, **60**, 102840.

23 T. Weigel, F. Schipper, E. M. Erickson, F. A. Susai, B. Markovsky and D. Aurbach, *ACS Energy Lett.*, 2019, **4**, 508–516.

24 A. Patel, S. Mallick, J. H. Mugumya, N. Lopez-Riveira, S. Kim, M. Jiang, M. P. Paranthaman, M. L. Rasche, H. Lopez and R. B. Gupta, *Mater. Today Energy*, 2024, **41**, 101545.

25 J. Zheng, Y. Ye, T. Liu, Y. Xiao, C. Wang, F. Wang and F. Pan, *Acc. Chem. Res.*, 2019, **52**, 2201–2209.

26 J. Zheng, G. Teng, C. Xin, Z. Zhuo, J. Liu, Q. Li, Z. Hu, M. Xu, S. Yan, W. Yang and F. Pan, *J. Phys. Chem. Lett.*, 2017, **8**, 5537–5542.

27 E. D. Orlova, A. A. Savina, S. A. Abakumov, A. V. Morozov and A. M. Abakumov, *Symmetry*, 2021, **13**, 1628.

28 Y. S. Meng, Y. W. Wu, B. J. Hwang, Y. Li and G. Ceder, *J. Electrochem. Soc.*, 2004, **151**, A1134.

29 D. Liu, Z. Wang and L. Chen, *Electrochim. Acta*, 2006, **51**, 4199–4203.

30 T. Weigel, F. Schipper, E. M. Erickson, F. A. Susai, B. Markovsky and D. Aurbach, *ACS Energy Lett.*, 2019, **4**, 508–516.

31 G. Zha, W. Hu, S. Agarwal, C. Ouyang, N. Hu and H. Hou, *Chem. Eng. J.*, 2021, **409**, 128343.

32 C. Mi, E. Han, L. Li, L. Zhu, F. Cheng and X. Dai, *Solid State Ionics*, 2018, **325**, 24–29.

33 C. Kim, T. J. Park, S. G. Min, S. Bin Yang and J. T. Son, *J. Korean Phys. Soc.*, 2014, **65**, 243–247.

34 F. Wu, G. T. Kim, M. Kuenzel, H. Zhang, J. Asenbauer, D. Geiger, U. Kaiser and S. Passerini, *Adv. Energy Mater.*, 2019, **9**, 1902445.

35 G. Zha, N. Hu, Y. Luo, F. Wang, R. Wu, Y. Li, H. Fu and X. Fu, *J. Taiwan Inst. Chem. Eng.*, 2023, **144**, 104730.

36 S. Park, C. Jo, H. J. Kim, S. Kim, S. T. Myung, H. K. Kang, H. Kim, J. Song, J. Yu and K. Kwon, *J. Alloys Compd.*, 2020, **835**, 155342.

37 J. H. Mugumya, S. Mallick, A. Patel, M. L. Rasche, A. V. Sakpal, E. D. Huchler, S. Kim, R. B. Gupta and M. Jiang, *J. Alloys Compd.*, 2024, **994**, 174720.

38 J. Jiang, H. Wu, L. Ni and M. Zou, *Process Saf. Environ. Prot.*, 2018, **120**, 87–96.

39 M. Mou and M. Jiang, *J. Pharm. Innov.*, 2020, **15**, 281–294.

40 M. Jiang, Z. Zhu, E. Jimenez, C. D. Papageorgiou, J. Waetzig, A. Hardy, M. Langston and R. D. Braatz, *Cryst. Growth Des.*, 2014, **14**, 851–860.

41 C. Yao, Y. Liu, S. Zhao, Z. Dong and G. Chen, *AIChE J.*, 2017, **63**, 1727–1739.

42 M. T. Kreutzer, F. Kapteijn, J. A. Moulijn and J. J. Heiszwolf, *Chem. Eng. Sci.*, 2005, **60**, 5895–5916.

43 M. L. Rasche, M. Jiang and R. D. Braatz, *Comput. Chem. Eng.*, 2016, **95**, 240–248.

44 A. M. Nightingale, T. W. Phillips, J. H. Bannock and J. C. de Mello, *Nat. Commun.*, 2014, **5**, 3777.

45 M. Mou, Dissertation, Virginia Commonwealth University, 2022.

46 M. Mou, A. Patel, S. Mallick, K. Jayanthi, X.-G. Sun, M. P. Paranthaman, S. Kothe, E. Baral, S. Saleh, J. H. Mugumya, M. L. Rasche, R. B. Gupta, H. Lopez and M. Jiang, *ACS Appl. Energy Mater.*, 2023, **6**, 3213–3224.

47 M. Mou, A. Patel, S. Mallick, B. P. Thapaliya, M. P. Paranthaman, J. H. Mugumya, M. L. Rasche, R. B. Gupta, S. Saleh, S. Kothe, E. Baral, G. P. Pandey, H. Lopez and M. Jiang, *ACS Omega*, 2022, **7**, 42408–42417.

48 M. Malik, K. H. Chan and G. Azimi, *Mater. Today Energy*, 2022, **28**, 101066.

49 J. H. Mugumya, M. L. Rasche, R. F. Rafferty, A. Patel, S. Mallick, M. Mou, J. A. Bobb, R. B. Gupta and M. Jiang, *Energy Fuels*, 2022, **36**, 12261–12270.

50 R. J. Gummow, M. M. Thackeray, W. I. F. David and S. Hull, *Mater. Res. Bull.*, 1992, **27**, 327–337.

51 J. Reimers, *Solid State Ionics*, 1993, **61**, 335–344.

52 J. R. Mueller-Neuhaus, R. A. Dunlap and J. R. Dahn, *J. Electrochem. Soc.*, 2000, **147**, 3598.

53 J. Wilcox, S. Patoux and M. Doeff, *J. Electrochem. Soc.*, 2009, **156**, A192.

54 S. He, R. Zhang, X. Han, Y. Zhou, C. Zheng, C. Li, X. Xue, Y. Chen, Z. Wu, J. Gan, L. She, F. Qi, Y. Liu, M. Zhang, W. Du, Y. Jiang, M. Gao and H. Pan, *Adv. Mater.*, 2025, 2413760.

55 W. Li, J. N. Reimers and J. R. Dahn, *Solid State Ionics*, 1993, **67**, 123–130.